Eur. Phys. J. A **7**, 491–502 (2000)

THE EUROPEAN PHYSICAL JOURNAL A

Tensor polarization of $^{12}C[2_1^+]$ in the $^{16}O(^{13}C,^{12}C)^{17}O$ reaction at 50 MeV

N. Ikeda[1,a], F. Nakamura[1], K. Mizuuchi[1], T. Sugimitsu[1], S. Teruyama[1], T. Okamoto[1], H. Fujita[2], S. Morinobu[1]

[1] Department of Physics, Kyushu University, Fukuoka 812-8581, Japan
[2] Daiichi College of Pharmaceutical Sciences, Fukuoka 815-8511, Japan

Received: 2 August 1999 / Revised version: 3 February 2000
Communicated by K. Nakai

Abstract. The $^{16}O(^{13}C,^{12}C)^{17}O$ reaction at 50 MeV has been investigated using the kinematical coincidence method. Polarization tensors t_{20} and t_{40} of $^{12}C[2_1^+]$ for the quantization axis taken along the direction of propagation have been measured by analyzing the energy spectrum of $^{12}C[2_1^+]$, modulated by the effect of γ ray emission. The deduced t_{40} values significantly deviate from zero, contrary to the prediction of the distorted-wave Born approximation theory based on one-step p shell neutron stripping without spin-dependent interactions. The phenomenological spin–orbit interaction necessary to reproduce the magnitude of measured t_{40} is found to be much larger than the folding model prediction. It is shown that the experimental polarization tensors as well as the cross sections can be reproduced by introducing multi-step processes involving excitations in ^{12}C and ^{13}C without introducing spin-dependent interactions.

PACS. 25.70.Hi Transfer reactions – 24.70.+s Polarization phenomena in reactions – 24.10.Eq Coupled-channel and distorted-wave models

1 Introduction

The heavy-ion induced one-nucleon transfer reactions below 10 MeV/u have been investigated for various colliding systems [1–7]. The angular distributions of the reaction cross sections have generally been reproduced reasonably well by the distorted-wave Born approximation (DWBA) calculation. In some cases, however, unrealistic optical potentials used to represent the nuclear interaction between the colliding nuclei have been used in the calculation; this was necessary to reproduce the experimental data [3–6].

Examples of such unrealistic cases may be seen in the spin–orbit interaction, which has often been required to be one or two orders of magnitudes larger than the predictions of the folding model. It has also been suggested that the spin–orbit potential can effectively be generated by the channel coupling effect. The recent experiments on polarized lithium induced one-nucleon transfer reactions [7] have demonstrated that the DWBA calculation is unable to reproduce the measured vector and tensor analyzing powers. In these cases the coupled channel (CC) model analysis, which takes into account the strong coupling between the ground and excited states of lithium, has been found successful in explaining all of the observables without introducing the spin–orbit potential.

These investigations imply that the successful description of the cross section alone may not be enough to justify the one-step DWBA analysis and that the spin observables may provide useful information to determine the actual reaction mechanisms. For the reactions with heavier projectiles than ^{7}Li, however, the only ones available have been the magnetic substate population of $^{15}N[3/2_1^-]$ in the ^{16}O induced reactions [4] and a further accumulation of data was desirable.

For studying the reaction mechanisms from the spin degrees of freedom, it is of special importance to examine those observables whose DWBA interpretation may not be obscured by the choice of the optical potential. Since, theoretically, the rank of the polarization tensors of the ejectile is determined by the reaction mechanisms assumed and the spin-dependent interactions adopted, the experimental observation of even higher rank tensors is of great interest to verify the assumptions. In particular, in the case that the nuclear spin of the ejectile is larger than the spin or orbital angular momentum transfer, the measurement of the ejectile polarization tensors provides crucial information. This is because the one-step DWBA without the spin-dependent interactions only predicts none-zero tensor values for some limited rank, independent of the potential parameters. A similar restriction of the DWBA to the rank of the tensor analyzing powers has been noticed by Turkiewicz et al. [8]. Their measurement, however, has not been accurate enough to prove the presence of the higher rank tensors. The other polarization measurements carried out so far have not paid due attention to this fact.

[a] e-mail: ikeda@nucl.phys.kyushu-u.ac.jp

In the present paper, the experimental study of the ^{16}O(^{13}C,^{12}C)^{17}O reaction at 50 MeV is presented. Emphasis was placed on the measurement of the polarization tensors of the ^{12}C[2^+_1] ejectile by using the γ ray recoil method. The one-step DWBA without spin-dependent interaction predicts non-vanishing polarization tensors up to the 3rd rank for the most likely mechanism of $p_{3/2}$ neutron stripping from ^{13}C. The present measurement, on the contrary, gave the first example to show the presence of a finite polarization tensor term of the 4th rank for the reaction.

In Sect. 2, the theoretical description of the polarization tensors is briefly presented together with the formulae to evaluate the tensors by the γ ray recoil method. The experimental procedure, the data analysis and the results are presented, respectively, in Sects. 3, 4 and 5. The DWBA and CC analyses of the experimental data are given in Sect. 6. Section 7 contains a summary and discussion.

2 Principle of the polarization tensor measurement

2.1 Rank of polarization tensors

For the reaction $A(a,b)B$, the polarization tensors t_{kq} of the ejected particle b are represented by transition matrices $T_{M_B M_b M_A M_a}$ by

$$t_{kq} = \sum_{M_B M_b M_A M_a} \{\hat{I}_b (-)^{I_b - M_b} \langle I_b I_b M_b + q \ -M_b | kq\rangle \times T_{M_B M_b M_A M_a} T^*_{M_B M_b + q M_A M_a}\} / \sum_{M_B M_b M_A M_a} |T_{M_B M_b M_A M_a}|^2,$$

with $0 \le k \le 2I_b$ [9]. The symbols I and M are used to represent, respectively, the spins and magnetic quantum numbers of the nuclei denoted by the subscripts, and $\hat{I}_b = (2I_b+1)^{1/2}$. Based on the DWBA theory (for example, see [2]), the transition matrices can be expressed as an expansion in the reduced amplitudes $\bar{t}^m_{l J_{ba} J_{BA}}$ in the absence of the spin-dependent interaction, where $m = M_B - M_A + M_b - M_a$. Here, we have expressed the angular momentum transfers by

$$\boldsymbol{J}_{ba} = \boldsymbol{I}_b - \boldsymbol{I}_a; \quad \boldsymbol{J}_{BA} = \boldsymbol{I}_B - \boldsymbol{I}_A; \quad \boldsymbol{l} = \boldsymbol{J}_{BA} + \boldsymbol{J}_{ba}.$$

The polarization tensors t_{kq} of the ejectile b are then expressed by

$$t_{kq} = \sum_{l l' J_{BA} J_{ba} J'_{ba}} \Big\{ \hat{J}_{ba} \hat{J}'_{ba} \hat{l} \hat{I}_b (-)^{J_{BA} - J_{ba} - J'_{ba} + I_a - I_b + l'} \times W(l l' J_{ba} J'_{ba}; k J_{BA}) W(I_b I_b J_{ba} J'_{ba}; k I_a) \times \sum_m \hat{k} \langle l k m q | l' m+q \rangle \bar{t}^m_{l J_{ba} J_{BA}} \bar{t}^{m+q\,*}_{l' J'_{ba} J_{BA}} \Big\} / \sum_{m l J_{BA} J_{ba}} |\bar{t}^m_{l J_{ba} J_{BA}}|^2.$$

From the properties of the Racah coefficient appearing in the equation we obtain a bound to k:

$$|J_{ba} - J'_{ba}| \le k \le J_{ba} + J'_{ba}.$$

The absence of the spin-dependent interaction leads, for the stripping reaction, to the fact that the total angular momentum $\boldsymbol{j_1}$ of the transferred particle in the nucleus a is equal to $-\boldsymbol{J}_{ba}$ [2,8]. In the case that only a unique value of j_1 is allowed and $j_1 \le I_b$, the limitation to the rank of the polarization tensor becomes $0 \le k \le 2j_1$.

The (^{13}C,^{12}C[2^+_1]) reaction has been predicted to be due to pure $p_{3/2}$ shell nucleon transfer from the shell model calculation by Cohen and Kurath [10]. If the spin-dependent interaction is negligibly small as predicted by the folding model, the tensor terms of rank $k > 3$ should be zero in the framework of DWBA. As a consequence, the one-step DWBA theory predicts that the 4th rank tensor terms of ^{12}C[2^+_1] are to be identically zero in the absence of a spin-dependent interaction.

2.2 Measurement of polarization tensors

The ejectile of the reaction, if it is left at an excited state, decays via γ ray emission in flight to cause a change in the kinetic energy of the nucleus depending on the angle of the emission. If, further, the nucleus is polarized, the γ ray emission probability is not isotropic, and the ejectile is expected to show some characteristic energy distribution which reflects the γ ray angular distribution.

The polarization tensors t_{kq} with even k and $q = 0$ of the γ decaying nucleus can be obtained by observing the modulation of the energy spectrum due to the recoil of the γ ray emission. This method, referred to as the γ ray recoil method, allows one to extract information of the angular distribution of the emitted γ ray with high efficiency.

Bohlen and von Oertzen [11] described the formulae to extract the polarization tensor terms t_{k0} of the decaying nucleus taking the z-axis along the direction of propagation in the laboratory frame. Sugiyama et al. [12] have pointed out that the t_{kq} elements with $q \neq 0$ which still remain in the equations of Bohlen and von Oertzen can be eliminated by taking the z-axis along the direction of propagation in the center-of-mass (c.m.) frame.

The γ ray recoil method has been successfully applied to the measurements where the high momentum resolving capabilities of the magnetic spectrographs are utilized [4, 11–13]. In this paper, we demonstrate that the simultaneous measurement of energy and scattering angle of the ejectile with a position sensitive silicon detector (PSD) also facilitates an alternative experiment to measure the polarization tensors by the γ ray recoil method.

The ejected particle before and after the γ ray emission is denoted by b and c, respectively. We express the momenta of the ejectile before and after the γ ray emission by $P_b(\Theta_b)$ and $P_c(\Theta_c)$, respectively, in the c.m. frame, with Θ representing the c.m. scattering angle. According

to [12], P_b and P_c are related by

$$P_c^2(\Theta_c) = \left(P_b\,(\Theta_b) - \frac{\beta_b + \cos\theta_\gamma}{(1-\beta_b^2)^{1/2}} P_\gamma \right)^2 + P_\gamma^2 \sin^2\theta_\gamma,$$

where β_b is the velocity of the particle b relative to the speed of light in the c.m. frame, P_γ the recoil momentum by the emission of the γ ray in the moving frame of b and θ_γ the polar angle of the γ ray emission measured from the z-axis taken along the direction of propagation of b. The momentum $P_b(\Theta_b)$ can be replaced by $P_b(\Theta_c)$ since the magnitude of the momentum of b in the c.m. system is independent of the scattering angle. Assuming that $P_\gamma/P_b \ll 1$ and $\beta_b^3 \ll 1$, the equation can be written in terms of the kinetic energies E_b and E_c of the particles as

$$\frac{\sqrt{1-\beta_b^2}}{\beta_b E_\gamma}(E_c(\Theta_c) - E_b(\Theta_c)) + \frac{1}{2}\beta_b = -\cos\theta_\gamma, \qquad (1)$$

where E_γ is the energy of the emitted γ ray.

The double differential cross section for the particle c is given by

$$\frac{\mathrm{d}^2\sigma}{\mathrm{d}\Omega_c \mathrm{d}E_c} = \frac{\mathrm{d}\sigma}{\mathrm{d}\Omega_b}(\Theta_b)\frac{\mathrm{d}\Omega_b}{\mathrm{d}\Omega_c}\frac{W(\Theta_b,\theta_\gamma,\phi_\gamma)}{4\pi}\frac{\mathrm{d}\Omega_\gamma}{\mathrm{d}E_c}, \qquad (2)$$

where W represents the γ ray emission probability per unit solid angle in the direction of polar angles (θ_γ, ϕ_γ) with the normalization of $\int W(\Theta_b,\theta_\gamma,\phi_\gamma)\mathrm{d}\Omega_\gamma = 4\pi$. Assuming that the angular change due to the γ ray emission is negligibly small, (2) can be written by replacing Θ_b by Θ_c as

$$\frac{\mathrm{d}^2\sigma}{\mathrm{d}\Omega_c \mathrm{d}E_c} = \frac{\mathrm{d}\sigma}{\mathrm{d}\Omega_b}(\Theta_c) \times \int_0^{2\pi} \frac{W(\Theta_c,\theta_\gamma,\phi_\gamma)}{4\pi}\sin\theta_\gamma \frac{\mathrm{d}\theta_\gamma}{\mathrm{d}E_c}\mathrm{d}\phi_\gamma. \qquad (3)$$

From (1) we obtain

$$\sin\theta_\gamma \frac{\mathrm{d}\theta_\gamma}{\mathrm{d}E_c} = \frac{\sqrt{1-\beta_b^2}}{\beta_b E_\gamma}.$$

Equation (3) is then expressed as

$$\frac{\mathrm{d}^2\sigma}{\mathrm{d}\Omega_c \mathrm{d}E_c} = \frac{\sqrt{1-\beta_b^2}}{\beta_b E_\gamma}\frac{\mathrm{d}\sigma}{\mathrm{d}\Omega_b}(\Theta_c) \times \int_0^{2\pi} \frac{W(\Theta_c,\theta_\gamma,\phi_\gamma)}{4\pi}\mathrm{d}\phi_\gamma. \qquad (4)$$

The γ ray emission probability $W(\Theta_c,\theta_\gamma,\phi_\gamma)$ can be written using the polarization tensors as [9]

$$W(\Theta_c,\theta_\gamma,\phi_\gamma) = \sum_{kq} A_k t_{kq} Y^*_{kq}(\theta_\gamma,\phi_\gamma).$$

Parity conservation in the γ decay requires A_k with odd k to be zero. It is obvious that the terms involving t_{kq} with $q \neq 0$ vanish when integrated over ϕ_γ, and (4) reduces to

$$\frac{\mathrm{d}^2\sigma}{\mathrm{d}\Omega_c \mathrm{d}E_c} = \frac{\sqrt{1-\beta_b^2}}{2\beta_b E_\gamma}\frac{\mathrm{d}\sigma}{\mathrm{d}\Omega_b}(\Theta_c)\sum_{k,\mathrm{even}} A_k t_{k0} P_k(\cos\theta_\gamma). \qquad (5)$$

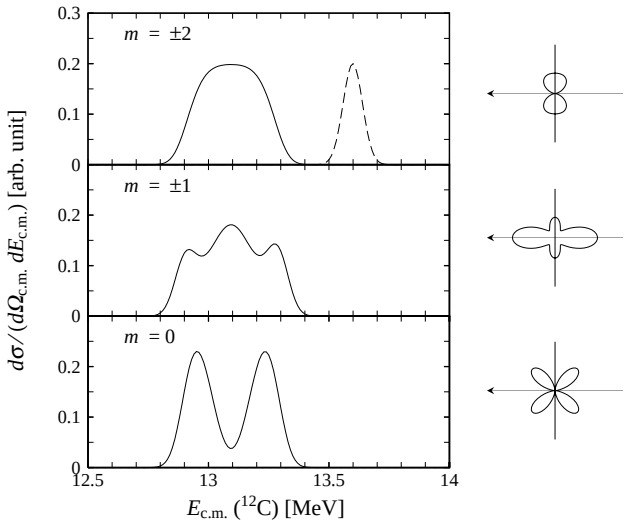

Fig. 1. Examples of the center-of-mass line shape of ^{12}C[2^+_1] for different m substates, calculated for the ^{16}O(^{13}C,^{12}C[2^+_1])^{17}O[g.s.] reaction at 50 MeV (folded with a Gaussian shaped instrumental response with a FWHM of 95 keV). The dashed line does not include the effect of broadening due to the recoil of the γ ray emission. The emission patterns of the γ ray are shown to the right

Equations (5) and (1) imply that the terms of t_{k0} with even k can be determined by measuring the energy and the emission angle of the particle c simultaneously. Such measurements may conveniently be made by using the conventional PSD for detecting particle c.

It may be illustrative of the effectiveness of the measurement to examine the energy spectrum of c for different m substates, in a similar manner as demonstrated in [11,12]. Figure 1 shows examples of the expected c.m. energy spectra in the ^{16}O(^{13}C,^{12}C[2^+_1])^{17}O[g.s.] reaction at 50 MeV. The spectra include the effect of the instrumental energy resolution of 95 keV in the c.m. frame, which is somewhat larger than the experimental value for the PSD used. The calculated line shapes are characteristic enough to allow the extraction of the m substate population, i.e. t_{20} and t_{40}, from the energy spectrum measurement.

3 Experiment

3.1 Experimental procedure

A target of SiO evaporated onto a carbon backing was irradiated by a ^{13}C beam of 50 MeV from the Kyushu University tandem accelerator. The target was placed perpendicular to the beam direction with the carbon backing side facing the incident beam. Both the ejectile and the residue were detected in coincidence using two one-dimensional PSDs. The ejected ^{12}C nuclei were measured by a PSD (PSD-E) of 100 μm in thickness and 45 mm $\times$8 mm in area, placed 150 mm apart from the target. For the ^{17}O residues, a 500 μm thick PSD (PSD-R) with an effective area of 45 mm $\times$7 mm was used at a distance of 115 mm from the target.

In the measurement of the $^{16}O(^{13}C,^{12}C[2_1^+])^{17}O$[g.s., 1st] and $^{16}O(^{13}C,^{12}C$[g.s.]$)^{17}O$[1st] reactions, it was important to be sure that the ^{12}C nuclei in the whole angular range covered by the PSD-E be detected in kinematical coincidence with the recoiling ^{17}O residues. For this purpose, a slit having an aperture of 36 mm in width and 2 mm in height was placed in front of the PSD-E, whereas no slit was used for the PSD-R. For correctly locating the beam with respect to the detectors, the vertical position of the beam on the target was adjusted so as to cause the maximal yield in the coincidence events. The PSD-E and the PSD-R covered the angular ranges of $14.2° \leq \theta_{lab} \leq 27.8°$ and $-66.0° \leq \theta_{lab} \leq -44.0°$, respectively.

A measurement with another set-up, covering the angular ranges of $12.2° \leq \theta_{lab} \leq 25.8°$ by the PSD-E and $-71.0° \leq \theta_{lab} \leq -49.0°$ by the PSD-R, was made to observe the $^{16}O(^{13}C,^{12}C$[g.s.]$)^{17}O$[g.s., 1st] reactions. In this case, the target foil was tilted by 10° so that the ^{17}O recoils would see the same target thickness as in the above measurement of the $(^{13}C,^{12}C[2_1^+])$ reactions. We also made a measurement of vertical distribution of the ^{17}O recoils by placing the PSD-R perpendicular to the reaction plane.

Additional single measurements of elastic scattering using the PSD-E were carried out from time to time to monitor the target thickness. The thicknesses of oxygen and silicon were estimated from the optical model analysis to be 5.9 and 6.0 $\mu g/cm^2$, respectively. The thickness of the carbon foil was estimated to be 17 $\mu g/cm^2$. It was found that the thicknesses of oxygen and silicon were constant during the experiment, while the carbon thickness increased linearly with the integrated beam charges due to the carbon build-up effect. The energy shifts of the oxygen recoils obtained in the coincidence measurement indicated that the carbon deposit grew equally on both the surfaces of the target foil. The irradiation spot on the target was changed at some times by vertically moving the target holder so that the total deposit of carbon did not exceed 12 $\mu g/cm^2$.

An auxiliary measurement for the cross section of the α transfer reaction $^{16}O(^{13}C,^{17}O)^{12}C[2_1^+]$ was also made at forward angles to see its contribution to the $^{16}O(^{13}C,$ $^{12}C[2_1^+])^{17}O$ measurement.

3.2 Examination of instrumental resolution

Since in the present experiment the information of both angles and energies of the particles is of crucial importance to extract the polarization tensors of $^{12}C[2_1^+]$, the performance of the detectors and the geometry of the experiment were carefully examined experimentally. The effect of the finite beam spot size on the target was also the subject of examination in determining the practical detector solid angles and energy resolution. For this purpose, elastic scattering of ^{13}C on ^{197}Au and the $^{16}O(^{13}C,^{12}C$[g.s.]$)^{17}O$[g.s.] reaction were used.

The PSDs were calibrated in position and energy using the elastic scattering of ^{13}C on gold. Two screens, each with 21 regularly spaced rectangular apertures were placed in front of the PSDs to geometrically define the position of particle incidence on the detector (i.e., particle emission angle from the target). From this measurement both of the PSDs were found to have an energy resolution of 135 keV in FWHM and an angular resolution of 0.03° for the 50 MeV ^{13}C particles.

To see the practical energy and angular resolutions for ^{12}C and ^{17}O, the coincidence data obtained (without the above-mentioned detector screens) in the experiment for the $^{16}O(^{13}C,^{12}C$[g.s.]$)^{17}O$[g.s.] reaction were examined. The deviations of energies and angles of ^{17}O from the kinematics calculation were calculated event by event assuming that the measured ^{12}C angles from the position on the PSD-E were correct. From the distribution of the energy deviation, the energy resolution for ^{17}O was found to be about 150 keV, almost independent of the measured ^{12}C angle. The ^{12}C energy resolution of the PSD-E was obtained by calculating the deviation of the measured energy from the kinematics calculation based on the measured ^{12}C angle. The resolution was obtained as a function of the ^{12}C angle to be typically around 150 keV in FWHM.

The derived ^{12}C energy resolution, which was somewhat larger than 135 keV as derived from the elastic scattering on gold, includes the error in the kinematics calculation due to the uncertainty in the measured ^{12}C emission angle. The angle uncertainty for ^{12}C which arises from the multiple scattering in the target was estimated using the formulae by Marion and Zimmerman [14] to be about 0.05° in FWHM, comparable to the angular resolution of the PSD-E. The multiple scattering effect and the finite position resolution of the PSD-E were estimated to be too small to cause the observed energy broadening of the ^{12}C. From this fact, the difference of the above resolution values was most plausibly attributed to the additional uncertainties in the ^{12}C angle arising from the finite beam spot size on the target. The FWHM beam width in the horizontal direction to reproduce the observed ^{12}C line shape was estimated to be 0.61 ± 0.05 mm assuming Gaussian shape for the beam intensity distribution and taking the $E^{1/2}$ dependence of the intrinsic energy resolution of the PSD into account.

The angular deviations of ^{17}O from the kinematics, as obtained in the above procedure for the PSD-R placed on and perpendicular to the reaction plane, also showed the effect of the finite beam width. The horizontal and vertical distributions of the ^{17}O angular deviations are compared in Fig. 2 at $\theta_{lab}(^{12}C) = 17.5° \pm 1.0°$. The difference between the horizontal and vertical angular spreads was due to the difference of the beam widths in the corresponding directions. Considering the angular spread caused by the vertical aperture of the PSD-E for ^{12}C, the FWHM beam width in the vertical direction to reproduce the data of Fig. 2 were obtained to be 1.2 ± 0.1 mm. The determined values of the FWHM beam widths in the horizontal and vertical directions were consistent with the observation of the beam profile during the experiment.

Figure 3 shows the FWHM horizontal angular spread as a function of the measured ^{17}O energy. The effect of the angle errors of ^{12}C caused by the multiple scattering, the angular resolution of the PSD-E and the finite beam

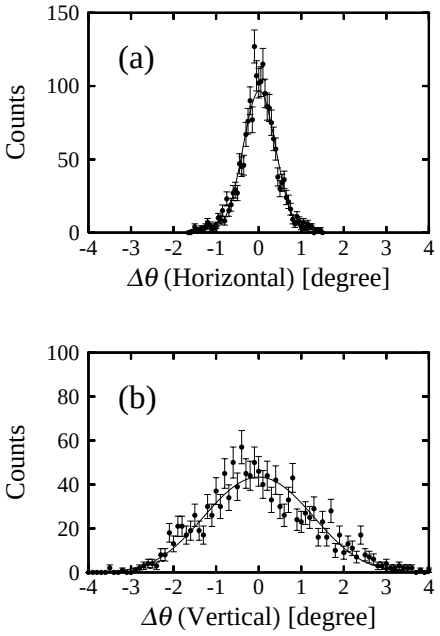

Fig. 2. The horizontal (a) and vertical (b) angular spreads of ^{17}O recoils from the $^{16}O(^{13}C,^{12}C[g.s.])^{17}O[g.s.]$ reaction at $\theta_{lab}(^{12}C)= 17.5°$, obtained as the angular deviations from the kinematics calculation. The solid lines represent the calculations taking the effects of the beam size on the target, the multiple scattering of ^{17}O in the target and the angular resolution of the PSD-R into account. The finite vertical aperture of the PSD for ^{12}C is also considered in the calculation (b)

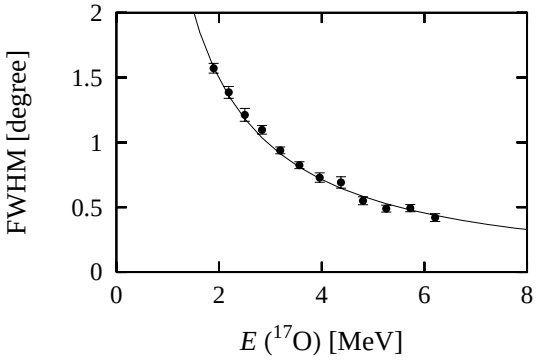

Fig. 3. The horizontal angular widths (FWHM) of the recoil nuclei from the $^{16}O(^{13}C,^{12}C[g.s.])^{17}O[g.s.]$ reaction as a function of the detection energy of ^{17}O. The solid line represents the calculation taking the effect of the multiple scattering of ^{17}O in the target and the angular resolution of the PSD-R into account

size were estimated to be negligible. As seen in Fig. 3, the FWHM of the horizontal angular spread of ^{17}O was found to be dominated by the multiple scattering effect and was well explained by the inclusion of the intrinsic resolution obtained from the separate measurement using a ^{241}Am α source in conjunction with the assumption of a $1/E$ dependence on the particle energy.

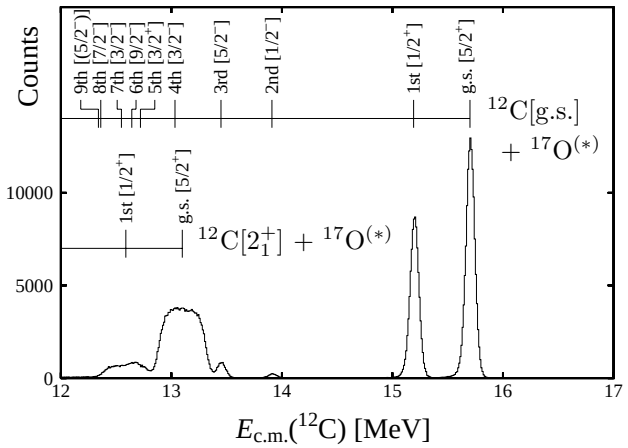

Fig. 4. Angle integrated center-of-mass energy spectrum of ^{12}C for the $^{16}O(^{13}C,^{12}C)^{17}O$ reaction. The lines and labels in the upper part denote the locations of the peaks leading to the ^{17}O excited states indicated

4 Data analysis

The individual reaction channels were satisfactorily identified by requiring the coincidence events to fall in the specified regions in the residue angle vs. ejectile angle ($\theta_R - \theta_E$) and the residue energy vs. ejectile angle ($E_R - \theta_E$) plots. The regions adopted for the selection were determined by considering the energy and angle uncertainties as described in Sect. 3.2 to accommodate more than 99% of the events of interest. The deviation from the two-body kinematics due to the γ ray emission was also taken into account in this procedure. For each event thus selected, the center-of-mass energy $E_{c.m.}$ of ^{12}C was calculated from the angle θ_{lab} and the energy E_{lab}, both of which were assumed to be correctly given by the measurement. Figure 4 shows the center-of-mass energy spectrum integrated over $15.5° \leq \theta_{lab} \leq 27.5°$. The energy broadenings due to the γ ray emission are clearly seen in the peaks corresponding to the $(^{13}C,^{12}C[2_1^+])$ reaction channels in the figure.

For examining the existence of contaminations from reactions other than $^{16}O(^{13}C,^{12}C)^{17}O$, the masses of the ejectiles (M_E) and the residues (M_R) were calculated event by event from the measured energies and angles using the two-body reaction kinematics. Figure 5 shows the two-dimensional plot of the calculated residue mass vs. the ejectile mass, for the events kinematically selected as of $^{16}O(^{13}C,^{12}C[2_1^+])^{17}O[g.s., 1st]$ in the above procedure (lower figure). Also shown is the similar plot for the events without the kinematical selection (upper figure). These plots indicate the absence of significant contribution from the other reaction channels to the broadened peaks of $^{16}O(^{13}C,^{12}C[2_1^+])^{17}O[g.s., 1st]$.

As seen in the center-of-mass energy spectrum in Fig. 4, the peaks corresponding to the $^{16}O(^{13}C, ^{12}C[2_1^+])^{17}O[g.s., 1st]$ reactions may include the contribution of the transitions to $^{12}C[g.s.]+^{17}O[4th to 9th]$. Since all these final states involve the neutron unbound states of ^{17}O, the contributions of the three-body reactions of $^{16}O(^{13}C,^{12}C)^{17}O^* \rightarrow ^{16}O+n$ to the recoil broadened peaks

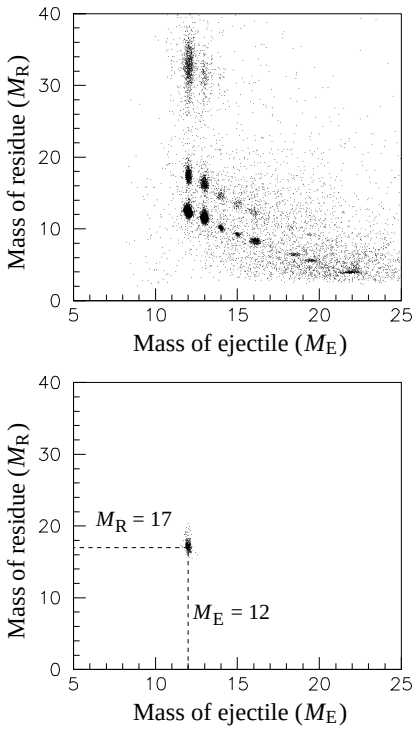

Fig. 5. The plots of the coincidence events (upper part) and the events selected for the $^{16}O(^{13}C,^{12}C[2_1^+])^{17}O$[g.s., 1st] reactions (lower part) in the residue mass vs. the ejectile mass

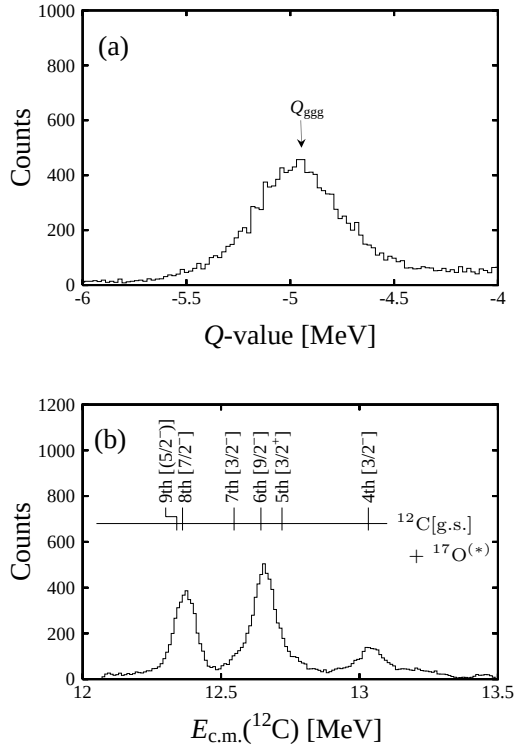

Fig. 6. (a) Three-body Q value spectrum and (b) center-of-mass energy spectrum of ^{12}C for $^{13}C+^{16}O \rightarrow ^{12}C+^{16}O+n$, integrated in the angular range of $15.5^\circ \leq \theta_{lab}(^{12}C) \leq 27.5^\circ$

were examined. The three-body components were identified by calculating three-body reaction Q values event-wise from the measured angles and the energies of the ejectiles and the residues.

The three-body Q value spectrum integrated over $15.5^\circ \leq \theta_{lab}(^{12}C) \leq 27.5^\circ$ is shown in Fig. 6a. Only the events for which neutrons were calculated to be emitted in a specified hemisphere in the moving frame of ^{17}O were selected to avoid the mixing of the transitions to $^{12}C[2_1^+]+^{17}O$[g.s., 1st]. A single peak centering at $Q_{ggg} = -4.947$ MeV for the reaction $^{13}C+^{16}O \rightarrow ^{12}C+^{16}O+n$ is clearly seen in this figure. Figure 6b shows the center-of-mass energy spectrum of ^{12}C reconstructed from the three-body events.

The contamination spectra in the $^{16}O(^{13}C,^{12}C[2_1^+])^{17}O$[1st] two-body spectrum (Fig. 7a), obtained by additionally requiring the calculated three-body Q values to fall between -4 MeV and -6 MeV, is shown in Fig. 7b. The events of $^{16}O(^{13}C,^{12}C$[g.s.])^{17}O[8th, 9th] succeeded by the γ decay were also collected (Fig. 7c) by requiring the events to fall in the corresponding regions in the θ_R - θ_E mapping. Comparing these spectra, the contributions of the three-body reactions $^{16}O(^{13}C,^{12}C$[g.s.])^{17}O[5th to 9th] $\rightarrow ^{16}O+n$ and the two-body reactions $^{16}O(^{13}C,^{12}C$[g.s.])^{17}O[8th, 9th] $\rightarrow ^{17}O+\gamma$(s) are obviously negligible.

The ^{12}C[g.s.]$+^{17}O$[4th] peak in the broadened peak of $^{12}C[2_1^+]+^{17}O$[g.s.] and the peaks of transitions to ^{12}C[g.s.]$+^{17}O$[5th to 7th] succeeded by the γ decay could not be extracted in the above procedure. However, the contributions of ^{12}C[g.s.]$+^{17}O$[5th, 7th] were likewise considered negligible from the relative intensities seen in Fig. 6b. In the following analysis, all these contaminations were basically ignored and the possible effects of those of $^{12}C+^{17}O$[4th] and $^{12}C+^{17}O$[6th] were examined in the peak profile analysis.

5 Analysis of recoil broadened ^{12}C line shape and polarization tensors

The ^{12}C line shape without the γ ray recoil broadening was estimated from those of the $^{16}O(^{13}C,$ ^{12}C[g.s.])^{17}O[g.s., 1st] reactions. As described above, the intrinsic energy resolution of the PSD, which varies as $E^{1/2}$, and the angle uncertainty caused by the finite size of the beam spot on the target were taken into account. The line shape was calculated in the laboratory frame as a function of ^{12}C energy in the laboratory frame and then transformed to the center-of-mass frame.

Since the detector geometry adopted was based on the consideration that all the ^{17}O recoils corresponding to the γ ray emitting ^{12}C ejectiles from the point source be detected without any loss, the vertical beam width and the multiple scattering were expected to cause some counting loss of ^{17}O depending on the polar angle of the γ ray emission from ^{12}C. In order to know the coincidence efficiency, a simulation was made, taking all these effects into account

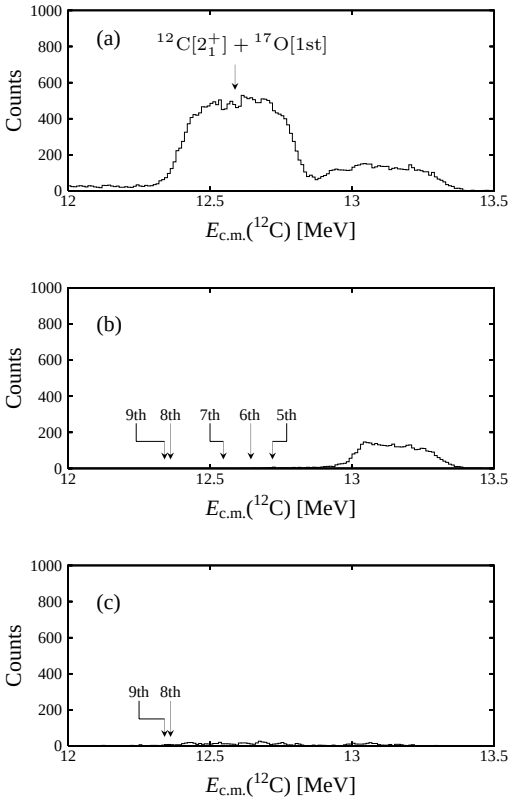

Fig. 7. (a) Angle integrated center-of-mass energy spectrum of ^{12}C for the ^{16}O(^{13}C,^{12}C[2^+_1])^{17}O[1st] reaction. (b) The contributions of the ^{16}O(^{13}C,^{12}C[g.s.])^{17}O* $\rightarrow ^{16}$O+n reactions in the spectrum (a). (c) The contributions of the ^{16}O(^{13}C,^{12}C[g.s.])^{17}O[8th, 9th] reactions followed by the γ ray emission

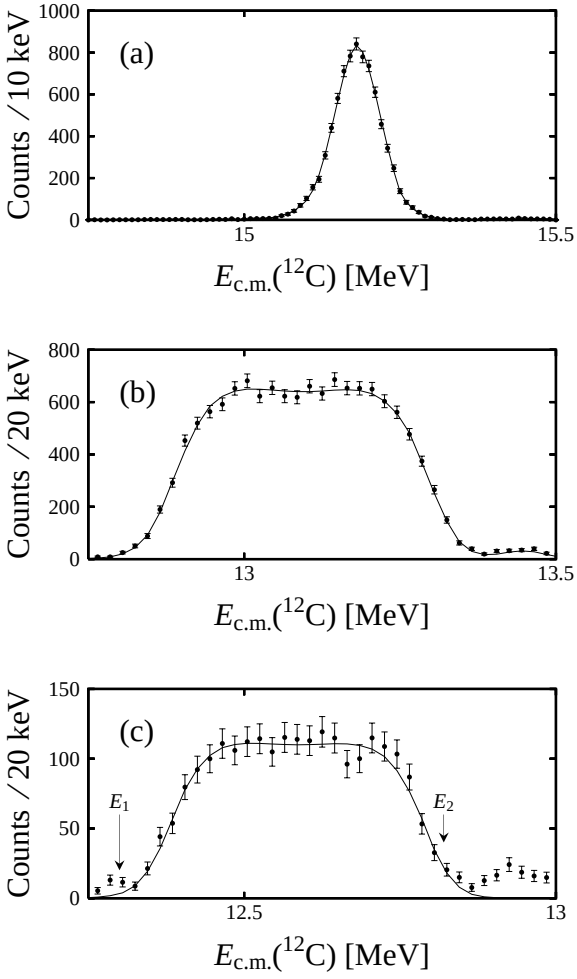

Fig. 8. The center-of-mass energy spectra at θ_{lab}(^{12}C) = 19° for the (a) ^{16}O(^{13}C,^{12}C[g.s.])^{17}O[1st], (b) ^{16}O(^{13}C,^{12}C[2^+_1])^{17}O[g.s.] and (c) ^{16}O(^{13}C,^{12}C[2^+_1])^{17}O[1st] reactions. The solid curves represent the fitted line shapes. For the ^{12}C[2^+_1]+^{17}O[1st] transition, the data in the region between E_1 and E_2 have been used in the fitting procedure

following the experimental observation in Sect. 3.2. The beam shape was assumed to be Gaussian and the γ ray emission probability to be independent of the azimuthal angle ϕ_γ. The estimated coincidence efficiencies for the ^{16}O(^{13}C,^{12}C[2^+_1])^{17}O[g.s., 1st] reactions were found to be in the range of 80 to 98%, depending on the detection angle θ_{lab} of ^{12}C. For a fixed θ_{lab}(^{12}C), the efficiency varied with θ_γ within 5%.

The least squares fit of (5), folded by the unbroadened line shape and multiplied by the coincidence efficiency, to the observed recoil broadened peak was carried out. Examples of the fits for the ^{16}O(^{13}C,^{12}C[2^+_1])^{17}O[g.s., 1st] reactions at $\theta_{lab} = 19°$ are shown in Fig. 8 together with the unbroadened peak profile. The fitting regions of the ^{12}C[2^+_1]+^{17}O[g.s.] spectra were chosen to include the small unbroadened ^{12}C+^{17}O[3th] transition and in the case of ^{12}C[2^+_1]+^{17}O[1st] to avoid the contamination from the ^{12}C[2^+_1]+^{17}O[g.s.] transition (see captions to Fig. 8). The fitting was performed for all the spectra at different center-of-mass angles $\Theta_{c.m.}$ with angle bins of $\Delta\Theta_{c.m.} = 1.8°$.

The derived t_{20} and t_{40} values and the cross sections are presented in Fig. 9 against the center-of-mass angle of ^{12}C. The fitting results clearly showed the presence of t_{40}. The assumption of the Gaussian shaped beam profile, which was used to estimate the coincidence efficiency, did not essentially affect the fitting results, and a change of the vertical beam width from 0 to 2 mm was found to cause shifts of ±0.01 and ±0.002 in the t_{20} and t_{40} values, respectively.

To examine the effect of the possible contamination of ^{12}C[g.s.]+^{17}O[4th] in the ^{12}C[2^+_1]+^{17}O[g.s.] channel and of ^{12}C[g.s.]+^{17}O[6th] in the ^{12}C[2^+_1]+^{17}O[1st] one, analyses which included their contributions as fitting parameters were also carried out. The contamination in the ^{12}C[2^+_1]+^{17}O[g.s.] channel was found to affect the result only negligibly and that in the ^{12}C[2^+_1]+^{17}O[1st] channel to shift the t_{20} and t_{40} values by no larger than the error limits presented in Fig. 9.

The inclusion of a finite t_{kq} with $q \neq 0$ was also examined by artificially introducing some finite values. This was because if the coincidence efficiency is not 100%, t_{kq} with $q \neq 0$ may not vanish in (5) due to the incomplete

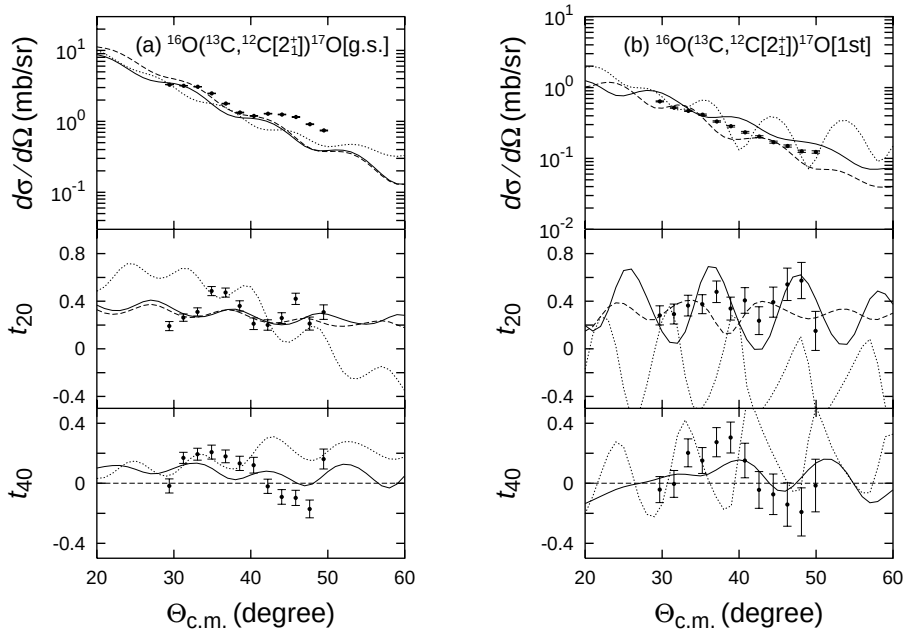

Fig. 9. Angular distributions of the cross sections, t_{20} and t_{40} for the (a) $^{16}O(^{13}C,^{12}C[2^+_1])^{17}O$[g.s.] and (b) $^{16}O(^{13}C,^{12}C[2^+_1])^{17}O$[1st] reactions. The dashed curves represent the one-step DWBA calculation without spin-dependent interactions. The dotted ones are the calculation introducing the $\boldsymbol{L}\cdot\boldsymbol{I_b}$ potential (see Sect. 6.1.2). The CC calculation with the spectroscopic amplitudes given in Table 2 is shown by solid lines

integration of (4) over ϕ_γ. The maximal shifts of t_{20} and t_{40} in this case were estimated to be less than their error limits for the possible presence of the finite t_{kq} with $q \neq 0$.

6 Theoretical analysis

The present data were compared with the DWBA and CC calculations using the codes TWOFNR [15] and FRESCO [16], respectively. In both calculations, the internal wavefunctions of the neutron were calculated using the Woods–Saxon type potentials with $r = 1.25$ fm, $a = 0.65$ fm and $V_{\rm s.o.} = 6.0$ MeV. The depths of the central potential were determined so as to reproduce the binding energies of the transferred neutron.

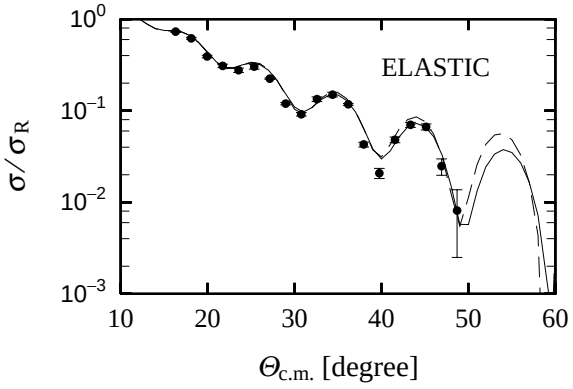

Fig. 10. Elastic scattering cross sections of ^{13}C on ^{16}O relative to the Rutherford ones. The dashed curve is the optical model calculation. The CC calculation is shown by a solid line

6.1 DWBA analysis

6.1.1 One-step DWBA prediction

The DWBA calculation was carried out assuming that only the one-step p shell neutron stripping process from ^{13}C contributes to the reactions. The optical potential parameters of Woods–Saxon form for the $^{13}C+^{16}O$ and $^{12}C+^{17}O$ systems as tabulated in Table 1 were obtained from the analysis of the elastic scattering data by Freeman et al. [17] using the optical model code SEARCH [18]. It was confirmed in Fig. 10 that the adopted optical potential in the entrance channel reproduces the measured elastic scattering angular distribution well. The spectroscopic amplitudes listed in Table 2 were determined so as to reproduce the magnitudes of the experimental cross sections with fixing the amplitude of $\nu(p_{1/2})\otimes^{12}C$[g.s.] configuration in ^{13}C[g.s.] at the value given by Cohen and Kurath [10].

Figure 11 shows the angular distributions of the cross sections of $^{16}O(^{13}C,^{12}C$[g.s.]$)^{17}O$[g.s., 1st] together with the DWBA predictions. For the transition to ^{17}O[g.s.], the calculation satisfactorily reproduces the measured angular distribution. The angular distribution calculated for

Table 1. Parameters of the optical model potential of Woods–Saxon form, used in the DWBA and CC calculations for the $^{16}O(^{13}C,^{12}C)^{17}O$ reaction

Channel		V	r_R	a_R	W	r_I	a_I	r_C
$^{13}C+^{16}O$	DWBA	94.5	1.19	0.44	11.6	1.26	0.21	1.45
	CC	94.5	1.17	0.47	11.6	1.26	0.21	1.45
^{12}C[g.s.]$+^{17}O$[g.s., 1st]	DWBA	87.7	1.11	0.61	19.1	1.35	0.28	1.45
$^{12}C[2_1^+]+^{17}O$[g.s., 1st]	DWBA	87.7	1.11	0.61	16.7	1.35	0.28	1.45
^{12}C[g.s., 2_1^+]$+^{17}O$[g.s., 1st]	CC	87.7	1.11	0.61	10.0	1.35	0.28	1.45

Table 2. Spectroscopic amplitudes used in the DWBA and CC calculations for the $^{16}O(^{13}C,^{12}C)^{17}O$ reaction

System	Neutron orbit (nlj)	Spectroscopic amplitude DWBA	CC
^{17}O[g.s.] $\rightarrow n+^{16}O$[g.s.]	$1d_{5/2}$	0.900	0.900
^{17}O[1st] $\rightarrow n+^{16}O$[g.s.]	$2s_{1/2}$	0.800	0.750
^{13}C[g.s.] $\rightarrow n+^{12}C$[g.s.]	$1p_{1/2}$	0.783	0.783
^{13}C[g.s.] $\rightarrow n+^{12}C[2_1^+]$	$1p_{3/2}$	−0.900 (−1.500 [a])	−0.600 [b]
$^{13}C[3/2_1^-] \rightarrow n+^{12}C$[g.s.]	$1p_{3/2}$		−0.433
$^{13}C[3/2_1^-] \rightarrow n+^{12}C[2_1^+]$	$1p_{1/2}$		−0.745 [b]
	$1p_{3/2}$		0.745
$^{13}C[5/2_1^-] \rightarrow n+^{12}C[2_1^+]$	$1p_{1/2}$		−0.745
	$1p_{3/2}$		0.745 [b]

[a] Value used in calculation when the spin–orbit potential is introduced.
[b] Opposite sign was used for input data to the code FRESCO for the internal consistency of the program.

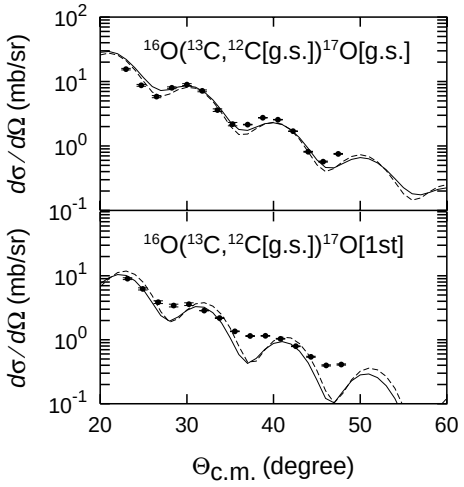

Fig. 11. Comparison of the measured cross sections of the $^{16}O(^{13}C,^{12}C$[g.s.]) reactions with the one-step DWBA (dashed lines) and CC (solid lines) calculations with the spectroscopic amplitudes listed in Table 2

^{17}O[1st] shows a too pronounced structure as compared with the experimental data.

The DWBA calculations for the $(^{13}C,^{12}C[2_1^+])$ reactions, presented in Fig. 9, reasonably reproduce the angular distributions of the cross sections and t_{20}. The possible contributions of the α transfer reactions $^{16}O(^{13}C,^{17}O)^{12}C[2_1^+]$ at backward angles to the $(^{13}C,^{12}C[2_1^+])$ one at forward angles were estimated to be three or four orders of magnitudes smaller than the experimentally observed cross sections. The estimation was made by normalizing the α transfer DWBA calculation to the measured cross sections at forward angles to give a rough order of magnitude of the backward angle cross sections.

The above results seem to justify the one-step DWBA analysis for the $(^{13}C,^{12}C[2_1^+])$ reactions. However, it is to be mentioned that the non-vanishing experimental t_{40} values clearly claim the defect of the present DWBA analysis, suggesting that t_{40} provides a sensitive tool for investigating the processes to be added to the single $p_{3/2}$ neutron stripping assumed.

6.1.2 Spin–orbit interaction

In the case that spin-dependent interactions between the colliding nuclei exist, the one-step DWBA predicts some finite t_{40} values for $^{12}C[2_1^+]$. Since the significance of the spin–orbit (s.o.) interaction has often been speculated in the heavy-ion induced one-nucleon transfer reactions [4–6], we examined the contributions of the $\boldsymbol{L}\cdot\boldsymbol{I}_a$ and $\boldsymbol{L}\cdot\boldsymbol{I}_b$ type interactions in the $A(a,b)B$ reaction. The $\boldsymbol{L}\cdot\boldsymbol{I}_B$ term was omitted since it only affects the spin orientation of the ^{17}O nucleus. The assumed interactions are of the form

$$V_{\text{s.o.}}(r) = V_{L\cdot I}\left(\frac{\hbar}{m_\pi c}\right)^2(\boldsymbol{L}\cdot\boldsymbol{I}) \times\frac{1}{r}\frac{\mathrm{d}}{\mathrm{d}r}\left\{\left[1+\exp\left(\frac{r-R_{\text{s.o.}}}{a_{\text{s.o.}}}\right)\right]^{-1}\right\}.$$

For the same geometrical parameters with those of the real central potential, the $\boldsymbol{L}\cdot\boldsymbol{I}_a$ and $\boldsymbol{L}\cdot\boldsymbol{I}_b$ interactions in the ranges of $0\,\mathrm{MeV} \leq V_{L\cdot I_a} \leq 10\,\mathrm{MeV}$ and $-20\,\mathrm{MeV} \leq V_{L\cdot I_b} \leq 10\,\mathrm{MeV}$ were not found to give t_{40} values larger than 0.05 for the ^{16}O(^{13}C,^{12}C[2^+_1])^{17}O[g.s.] reaction at $\Theta_{\mathrm{c.m.}} = 35°$. We examined the effect of the geometrical parameters to find that the t_{40} values comparable in magnitude with the experiment can be predicted when the radius parameter is set larger than that of the real central potential. For example, the $\boldsymbol{L}\cdot\boldsymbol{I}_b$ potential with a depth of 6 MeV, $r_{\mathrm{s.o.}} = 1.45\,\mathrm{fm}$ and $a_{\mathrm{s.o.}} = 0.5\,\mathrm{fm}$ gives the t_{40} values shown in Fig. 9 without introducing the $\boldsymbol{L}\cdot\boldsymbol{I}_a$ interaction. However, the calculation still fails to reproduce the angular distributions of t_{40}. The reproducibility of t_{20} becomes worse when compared with the calculation without the s.o. interactions.

So far, no prediction of the folding potential for ^{12}C[2^+_1]+^{17}O has been available. The s.o. potential derived for ^{13}C+^{139}Ba from the analysis of the ^{138}Ba(^{14}C,^{13}C)^{139}Ba reaction ($V_{L\cdot I} = 3\,\mathrm{MeV}$, $r_{\mathrm{s.o.}} = 1.45\,\mathrm{fm}$ and $a_{\mathrm{s.o.}} = 0.5\,\mathrm{fm}$) has been suggested to be a factor of 200 stronger than the folding model prediction [5]. This, together with the theoretical expectation that the folding model s.o. interaction is inversely proportional to the reduced mass times the projectile spin [19], leads to an estimation that the strength of the s.o. potential presently obtained would be about 600 times larger than the folding model prediction. Therefore, it would be unrealistic to attribute the non-vanishing t_{40} values to the s.o. interaction.

6.2 CC analysis

The phenomenological spin–orbit potentials have often been interpreted to arise from the effects of the couplings between the ground and excited states or of the reorientation couplings [5–7]. The above-mentioned strong $\boldsymbol{L}\cdot\boldsymbol{I}_b$ interaction may suggest a significant contribution of the couplings in which the ^{12}C[2^+_1] state participates. The contribution of the couplings between the ground state and the $3/2^-_1$ and $5/2^-_1$ excited states in ^{13}C may also be of importance since these excited states are considered to be mainly of a neutron coupled with a ^{12}C core in the 2^+_1 state. To investigate the coupling effects on the polarization tensors and the cross sections, a calculation with the couplings between the states in ^{12}C and ^{13}C was performed. The coupling and transfer mechanisms considered in the calculation are illustrated in Fig. 12.

The deformation length (δ_2) and the Coulomb matrix element (M(E2), see [16]) used for the excitation of ^{12}C were obtained from the reported B(E2) value of $42.0e^2\,\mathrm{fm}^4$ [20]. The parameters for the reorientation of ^{12}C[2^+_1] were set consistently following the prescription by Carter et al. [21]. The coupling parameters for ^{13}C were derived from the quadrupole deformation parameter of −0.428 found in the t+^{13}C inelastic scattering [22]. The optical model parameters for the ^{13}C+^{16}O and ^{12}C+^{17}O systems were so determined that the CC calculation reproduces the measured cross sections of the elastic scattering (Fig. 10) and the data of the elastic and inelastic scatterings in [17,23]. The optical model and deformation parameters used are summarized in Tables 1 and 3, respectively.

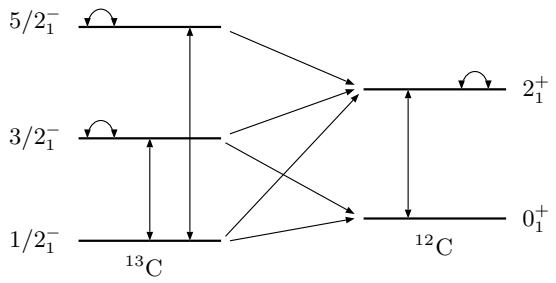

Fig. 12. Coupling and transfer processes considered in the calculation

Table 3. Coupling strength parameters adopted in the CC calculations

Nucleus	Transition	δ_2 (fm)	M(E2) ($e\,\mathrm{fm}^2$)
^{12}C	$0^+_1 \to 2^+_1$	−1.480	−6.481
^{12}C	$2^+_1 \to 2^+_1$	−1.480	7.746
^{13}C	$1/2^-_1 \to 3/2^-_1$	−1.207	−6.381
^{13}C	$3/2^-_1 \to 3/2^-_1$	−1.207	6.381
^{13}C	$1/2^-_1 \to 5/2^-_1$	−1.207	−7.807
^{13}C	$5/2^-_1 \to 5/2^-_1$	−1.207	8.346

The calculation was made fixing the spectroscopic amplitudes of n+^{12}C[g.s] at the values given in Table 2. The magnitudes of the n+^{12}C[2^+_1] amplitudes in ^{13}C[$3/2^-_1$] were taken from [24] and the same values were tentatively adopted for ^{13}C[$5/2^-_1$]. The results of the CC calculation with the spectroscopic amplitudes in Table 2 are shown as the solid lines in Figs. 9 and 11. The CC calculation gives the similar angular distributions of the cross sections of ^{16}O(^{13}C,^{12}C[g.s.])^{17}O[g.s., 1st] to the DWBA calculation. For the (^{13}C,^{12}C[2^+_1]) reactions, the CC calculation describes the cross sections and t_{20} as reasonably as the DWBA prediction without the spin-dependent interactions. A significant difference between the CC and the DWBA can be seen in the t_{40} values of ^{12}C[2^+_1]. The CC calculation shows a remarkably improved reproducibility for the t_{40} data.

To investigate the contributions of the multi-step processes in detail, the calculations were carried out omitting the neutron transfer process from ^{13}C[g.s.] to ^{12}C[g.s.] and/or those from the excited states of ^{13}C to ^{12}C[2^+_1]. As shown in Fig. 13, the CC calculations produce much smaller t_{40} values if we assume that the transfer reaction only takes place to ^{12}C[2^+_1] (dashed and dot-dashed lines). This suggests that the multi-step process passing through ^{12}C[g.s.], i.e. involving the excitation of ^{12}C, plays an essential role to cause the non-zero t_{40} values for ^{12}C[2^+_1].

It is also to be noted in Fig. 13, that the calculation, which includes the important process via ^{12}C[g.s.], gives a wrong sign for t_{40}, when the relative sign of the

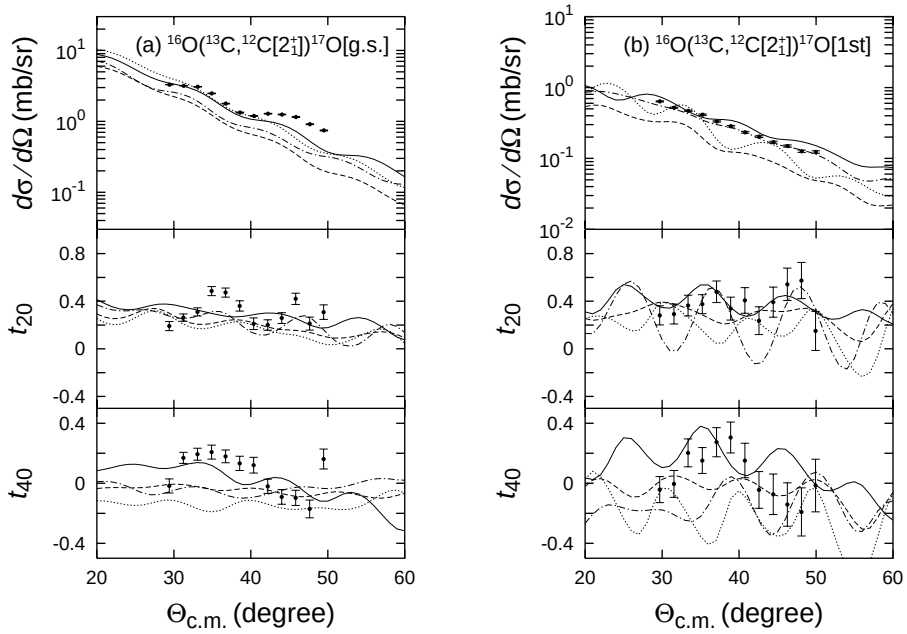

Fig. 13. CC calculations for ^{12}C[2^+_1] omitting either the transfer process from ^{13}C[g.s] to ^{12}C[g.s.] (dot-dashed lines) or those from ^{13}C[$3/2^-_1$, $5/2^-_1$] to ^{12}C[2^+_1] (solid lines), and the calculation with only introducing the transfer process from ^{13}C[g.s] to ^{12}C[2^+_1] (dashed lines). Also shown is the calculation with the n+^{12}C[2^+_1] amplitudes of 0.85 (opposite in sign to Table 2) for ^{13}C[g.s.] and 0 for ^{13}C[$3/2^-_1$, $5/2^-_1$] (dotted lines)

n+^{12}C[2^+_1] and n+^{12}C[g.s] spectroscopic amplitude for ^{13}C[g.s.] is reversed (dotted lines). In this case, addition of the transfer processes from ^{13}C[$3/2^-_1$, $5/2^-_1$] was found to be unable to predict the magnitudes of t_{40} for ^{16}O(^{13}C,^{12}C[2^+_1])^{17}O[g.s.], irrespective of the signs of the spectroscopic amplitudes for the excited states of ^{13}C (not shown in the figure). These observations suggest that t_{40} may serve to determine the sign of the n+^{12}C[2^+_1] spectroscopic amplitude relative to that of n+^{12}C[g.s.] for ^{13}C[g.s.].

The angular distributions of the polarization tensors are also influenced by the sign of the n+^{12}C[2^+_1] spectroscopic amplitudes for the excited states in ^{13}C. It was confirmed that the calculation with the signs of the amplitudes for ^{13}C[$3/2^-_1$, $5/2^-_1$] given in Table 2 gives the best description of the experimental data. Since, however, the tensor terms are seen to be less sensitive to the transfer processes from the excited states of ^{13}C than that from ^{13}C[g.s.], the definitive claim for the sign of the spectroscopic amplitudes for ^{13}C[$3/2^-_1$, $5/2^-_1$] seems to be difficult to make.

Although the calculations were also examined for different magnitudes of the spectroscopic amplitudes for ^{13}C [$3/2^-_1$, $5/2^-_1$], the better description of the data could not be obtained. We further examined the effects of the couplings between the elastic and inelastic channels to the excited states of ^{16}O and ^{17}O. None of the couplings were found to cause a sizable modification in the prediction for the t_{40} values.

7 Summary and discussion

The ^{16}O(^{13}C,^{12}C)^{17}O reaction at an incident energy of 50 MeV was studied experimentally. The measurements were carried out by detecting both the ejectiles and the residual nuclei using two one-dimensional PSDs. The reaction channels were well resolved using the kinematical relations of the two-body and three-body reactions. From the line shapes of the ^{12}C[2^+_1] particles broadened due to the γ ray emission, the polarization tensors t_{20} and t_{40} of ^{12}C[2^+_1] with the quantization axis taken along the direction of propagation were obtained. The polarization tensor elements have been shown to make a good probe for the inherent reaction mechanisms by contrast with the fact that the one-step DWBA calculation without the spin-dependent interactions predicts vanishing values.

The experimental t_{40} values deduced for the ^{16}O(^{13}C, ^{12}C[2^+_1])^{17}O[g.s., 1st] reactions largely deviated from zero. The phenomenological spin–orbit potential necessary to reproduce the experimental t_{40} values turned out to be much stronger than the folding model prediction. The experimental data were found to be reasonably reproduced by the calculations taking the couplings between the ground and excited states of ^{12}C and ^{13}C into account. The multi-step process passing through ^{12}C[g.s.] was considered to be the most important mechanism to cause non-zero values of t_{40}. The signs of the spectroscopic amplitudes of the $\nu(p_{1/2})\otimes^{12}$C[g.s.] and $\nu(p_{3/2})\otimes^{12}$C[2^+_1] configurations in ^{13}C[g.s.] were found to be opposite with each other to correctly predict the measured t_{40} values.

It should be noted that, if one diverts attention from the t_{40} values, the one-step DWBA would be considered successful in describing the reactions. The present investigation has revealed that the reproducibility of the cross sections and t_{20} is not enough to justify the DWBA, and the 4th rank polarization tensor provides crucial information to determine the actual reaction mechanisms.

The spectroscopic factors (squares of the spectroscopic amplitudes) of ^{13}C[g.s.] used in the DWBA calculation without the spin-dependent interactions were in reasonable agreement with the values derived from the DWBA analysis of the $^{13}C(p,d)^{12}C$ reaction [25,26]. However, the present coupled channel calculation predicts that the spectroscopic factor of $n+^{12}C[2_1^+]$ relative to that of $n+^{12}C$[g.s.] should be about one-half of the value from the DWBA analysis. This may imply that the multi-step processes involving the excitations of ^{12}C and ^{13}C also significantly contribute to the proton induced reaction. The investigation of the higher rank tensors of $^{12}C[2_1^+]$ for the light-ion induced transfer reactions on ^{13}C would be of interest to shed a new light upon this problem.

The authors wish to thank Mr. Y. Koga and Mr. T. Maeda for their excellent technical support. The present work was partly supported by a Grant-in-Aid for Encouragement of Young Scientists (Grant-in-Aid No. 08740210) of the Japanese Ministry of Education, Science, Sports and Culture.

References

1. R. Bass, Nuclear reactions with heavy ions (Springer-Verlag, Berlin, Heidelberg 1980), and references therein
2. G.R. Satchler, Direct nuclear reactions (Oxford University Press 1983), and references therein
3. T. Tamura, T. Udagawa, M.C. Mermaz, Phys. Rep. **65**, 345 (1980)
4. P. Wust, W. von Oertzen, H. Ossenbrink, H. Lettau, H.G. Bohlen, W. Saathoff, C.A. Wiedner, Z. Phys. A **291**, 151 (1979);
   P. Wust, W. von Oertzen, H. Ossenbrink, H. Lettau, H.G. Bohlen, W. Saathof, K. Wannebo, C.A. Wiedner, Phys. Lett. B **80**, 208 (1979)
5. W. von Oertzen, E.R. Flynn, J.C. Peng, J.W. Sunier, R.E. Brown, Z. Phys. A **310**, 275 (1983)
6. W. von Oertzen, H. Lettau, H.G. Bohlen, D. Fick, Z. Phys. A **315**, 81 (1984)
7. D. Fick, G. Grawert, I.M. Turkiewicz, Phys. Rep. **214**, 1 (1992), and references therein
8. I.M. Turkiewicz, Z. Moroz, K. Rusek, I.J. Thompson, R. Butsch, D. Krämer, W. Ott, E. Steffens, G. Tungate, K. Becker, K. Blatt, H.J. Jänsch, H. Leucker, D. Fick, Nucl. Phys. A **486**, 152 (1988)
9. M. Simonius, Lecture notes in physics **30**, 38 (Springer, Berlin, Heidelberg 1974)
10. S. Cohen, D. Kurath, Nucl. Phys. A **101**, 1 (1967)
11. H.G. Bohlen, W. von Oertzen, Z. Phys. A **285**, 371 (1978)
12. Y. Sugiyama, Y. Tomita, H. Ikezoe, N. Shikazono, Z. Phys. A **322**, 579 (1985)
13. H.G. Bohlen, H. Ossenbrink, W. von Oertzen, P. Wust, H. Hafner, K. Wannebo, Z. Phys. A **285**, 379 (1978)
14. J.B. Marion, B.A. Zimmerman, Nucl. Instr. and Meth. **51**, 93 (1967)
15. M. Igarashi, computer code TWOFNR (private communication)
16. I.J. Thompson, Comput. Phys. Rep. **7**, 167 (1988)
17. R.M. Freeman, F. Haas, A. Morsad, C. Beck, Phys. Rev. C **39**, 1335 (1989)
18. T. Wada, optical model computer code SEARCH (unpublished)
19. F. Petrovich, D. Stanley, L.A. Parks, P. Nagel, Phys. Rev. C **17**, 1642 (1978)
20. P.H. Stelson, L. Grodzins, Nucl. Data Tables A **1**, 21 (1965)
21. J. Carter, Z.Z. Valakazi, R.W. Fearick, V. Hnizdo, E. Muskat, K.W. Kemper, D.E. Trcka, A.P Van Verst, Nucl. Phys. A **591**, 349 (1995)
22. P.J. Simmonds, K.I. Pearce, P.R. Hayes, N.M. Clarke, R.J. Griffiths, M.C. Mannion, C.A. Ogilvie, Nucl. Phys. A **482**, 653 (1988)
23. R.M. Freeman, C. Beck, F. Haas, A. Morsad, N. Cindro, Phys. Rev. C **33**, 1275 (1986)
24. V.A. Ziman, A.T. Rudchik, A. Budzanowski, V.K. Chernievsky, L. Głowacka, E.I. Koshchy, S. Kliczewski, M. Makowska-Rzeszutko, A.V. Mokhnach, O.A. Momotyuk, O.A. Ponkratenko, R. Siudak, I. Skwirczyńska, A. Szczurek, J. Turkiewicz, Nucl. Phys. A **624**, 459 (1997)
25. H. Taketani, J. Muto, H. Yamaguchi, J. Kokame, Phys. Lett. B **27**, 625 (1968)
26. P.R. Lewis, G.G. Shute, B.M. Spicer, V.C. Officer, P.R. Andrews, S.M. Banks, Nucl. Phys. A **474**, 499 (1987)